New particle formation event detection with convolutional neural networks

Xun Zhang [a,b], Lijie Wu [a], Xiansheng Liu [c,*], Tao Wang [d], Marta Monge [c],
Meritxell Garcia-Marlès [c,e], Marjan Savadkoohi [c,f], Imre Salma [g], Susanne Bastian [h],
Maik Merkel [i], Kay Weinhold [i], Alfred Wiedensohler [i], Holger Gerwig [j], Jean Putaud [k],
Sebastiao Martins Dos Dantos [k], Jakub Ondracek [l], Nadezda Zikova [l], Andrea Minkos [m],
Marco Pandolfi [c], Andrés Alastuey [c], Xavier Querol [c]

[a] Beijing Key Laboratory of Big Data Technology for Food Safety, School of Computer Science and Engineering, Beijing Technology and Business University, Beijing, China
[b] State Key Laboratory of Resources and Environmental Information System, Beijing, China
[c] Institute of Environmental Assessment and Water Research (IDAEA-CSIC), Barcelona, Spain
[d] Shanghai Key Laboratory of Atmospheric Particle Pollution and Prevention, Department of Environmental Science & Engineering, Fudan University, Shanghai, China
[e] Department of Applied Physics-Meteorology, University of Barcelona, Barcelona, Spain
[f] Department of Mining, Industrial and ICT Engineering (EMIT), Manresa School of Engineering (EPSEM), Universitat Politècnica de Catalunya (UPC), 08242 Manresa, Spain
[g] Institute of Chemistry, Eötvös Loránd University, Budapest, Hungary
[h] Saxon State Office for Environment, Agriculture and Geology (LfULG), Dresden, Germany
[i] Leibniz Institute for Tropospheric Research (TROPOS), Leipzig, Germany
[j] German Environment Agency (UBA), Dessau-Roßlau, Germany
[k] European Commission, Joint Research Centre (JRC), Ispra, Italy
[l] Institute of Chemical Process Fundamentals, Academy of Sciences of the Czech Republic Rozvojova, Prague, Czech Republic
[m] Department of Meteorology, Institute of Geography and Earth Sciences, Eötvös Loránd University, Budapest, Hungary

HIGHLIGHTS

- Employed ConvNeXt model, used transfer learning to identify NPF events.
- Comparative analysis showed ConvNeXt's outstanding 95.3% accuracy.
- Tests with different ConvNeXt variants demonstrated enhanced capabilities.
- ConvNeXt-XL excelled, achieving 96.4% accuracy in generalization experiments.

ARTICLE INFO

ABSTRACT

New aerosol particle formation (NPF) events play a significant role in altering aerosol concentrations and dispersion within the atmosphere, making them vital for both climate and air quality research. The primary objective of investigating NPF events is to precisely determine their occurrence dates. In this study, we introduced the ConvNeXt model for the first time to identify NPF events, and compared its performance with two other deep learning models, EfficientNet and Swin Transformer. Our main aim was to automate an objective identification and classification of NPF events accurately. All three models employed transfer learning to effectively capture critical features associated with NPF. Our results demonstrated that the ConvNeXt model significantly outperformed the other models, achieving an impressive accuracy rate of 95.3% on event days, surpassing EfficientNet (92.8%) and Swin Transformer (94.9%). Furthermore, we performed tests using different ConvNeXt variants (ConvNeXt-T/S/B/L/XL) and different pre-training weights, revealing that different configurations of ConvNeXt models exhibited improved NPF event recognition capabilities. Finally, we conducted generalizability experiments using the ConvNeXt-XL model, achieving the highest accuracy of 96.4% on event days. This study not only underscores the recognition prowess of ConvNeXt models but also highlights their practical utility in accurately detecting NPF events in real-world scenarios. This contribution aids in advancing

---

* Corresponding author.
E-mail address: liugar@cid.csic.es (X. Liu).

our comprehension of aerosol dynamics in atmospheric environments, providing valuable insights for climate and air quality research.

1. Introduction

The impact of aerosol particles on air quality (AQ), human health, and the global climate has been widely studied and recognized (Lelieveld et al., 2019; Luo et al., 2020; Rosenfeld et al., 2008; Zhang et al., 2019). For instance, aerosol exposure can increase cardiovascular and respiratory health effect in humans (Trechera et al., 2023; WHO, 2021). Furthermore, atmospheric aerosols play an important role in influencing global radiative forcing and climate impacts (Zhong et al., 2017), thus garnering significant attention on a global scale. Currently, there is a wealth of observations regarding aerosol number concentrations and their size distributions worldwide (Alonso-Blanco et al., 2018; Carnerero et al., 2021; Trechera et al., 2023), with new particle formation (NPF) being a substantial contributor to atmospheric aerosol particles, accounting for at least 50% of particles in the global atmosphere (Wang et al., 2015; H.B. Xie et al., 2017; Zhang et al., 2012).

The process of NPF can be divided into two main steps: homogeneous nucleation and growth (Kulmala et al., 2006). Nucleation involves the combination of atmospheric gas-phase vapors, such as sulphuric acid, ammonia, amines, and low volatility organic compounds, which undergo a gas-particle conversion process to form molecular clusters (Kulmala et al., 2000; Lehtipalo et al., 2018; Napari et al., 2002). Subsequently, these molecular clusters can be affected by further collisions of molecules until the cluster is thermodynamically stabilized and a new aerosol particle is born. The particle can further grow continuously mainly by condensation of additional vapors and coagulation, leading to increase in particle diameter (Cai and Jiang, 2017; Kulmala et al., 2013; Yue et al., 2010). During regional NPF events, a distinct "banana" shape appears in the particle number size distribution (PNSD) surface plot. The processes of NPF play a significant role in the atmospheric environment and have important implications for AQ (Du et al., 2021), cloud physics (Park et al., 2021), global radiation balance (Kulmala, 2003), and human health (Zhang, 2010). These events are highly affecting the levels of ultrafine particles (UFP) under different environmental conditions, as documented in diverse settings worldwide (Beck et al., 2021; Kecorius et al., 2015; Salma et al., 2021; Lihavainen et al., 2003; Pierce et al., 2014). For example, in the Pearl River Delta Region of China, secondary formation provides 72% of the particle number concentration (PNC) and 79% of the mass concentration (Chu et al., 2019). Moreover, NPF events pose a major uncertainty that holds primary importance in global climate modeling and prediction issues (Almeida et al., 2013; Ehn et al., 2014; Wang et al., 2015; Zhang et al., 2004).

The investigation of regional NPF events typically begins with the identification of whether an NPF event has occurred. Current research on NPF event detection can be categorized into three main approaches: manual-based, rule-based, and data-based. In the manual-based approach, researchers classify NPF events based on specific features observed in the PNSD map on a daily basis (DAL MASO et al., 2005; Hamed et al., 2007; Vana et al., 2008). This approach allows experts to visually distinguish regions on the graph that indicate the presence of an NPF event (Kulmala et al., 2012). However, the manual-based approach is labor-intensive, time-consuming, and subjective due to potential human bias. The rule-based approach involves classifying NPF events using predefined steps and thresholds of PNC as prior knowledge, which enables automatic classification of NPF events (Dada et al., 2018; Kulmala et al., 2012). However, PNC can vary significantly across different environments, making prior knowledge obtained from one site unreliable in other sites or complex scenarios. Data-based methods employ models that automatically identify NPF events based on measured PNSD data and labeled annotations of NPF event types (Joutsensaari et al., 2018; Su et al., 2022; Zaidan et al., 2018). The advantage of using neural networks (NNs) in data-based approaches is that they do not rely on specific PNC thresholds and can perform automatic classification, offering potential for deeper understanding and addressing aerosol-related issues in the atmospheric environment. Although previous studies have demonstrated the feasibility of image classification methods for NPF event detection, there is still room for improvement in classification accuracy, and the generalization performance of the models remains unsatisfactory. For example, Joutsensaari et al. (2018) achieved an accuracy of only 80% for event day classification, while Zaidan et al. (2018) reported an accuracy of 84.2%. In the study by Su et al. (2022), the accuracy of their model decreased as the objectivity score increased when using intensity segmentation to identify NPF event days. For instance, with an objectivity score of 0.2, the accuracy for event days was 90.6%. Additionally, there is a limited number of studies utilizing deep learning methods for NPF event detection, and robust model testing is lacking in the existing literature. Meanwhile, the source apportionment methods also allow detecting hourly source components of specific UFP sources (including PNC), and this also allows detecting NPF events. These methods are based on source apportionment analysis using reception modes such as positive matrix factorization (PMF) (Vörösmarty et al., 2024; Hopke et al., 2022 and references therein; Rivas et al., 2020) and clustering analysis (Salimi et al., 2014).

In this study, a pre-trained NN model is used to automatically classify NPF events through migration learning. We screened the EfficientNet model (Tan and V. Le, 2020), Swin Transformer model (Liu et al., 2021), and ConvNeXt model (Liu et al., 2022) by their performance on the ImageNet dataset (Deng et al., 2009), then compared their performance in the NPF event classification task. This study offers a more accurate solution for the classification of NPF events, contributing to a better understanding of the performance advantages exhibited by various NN models in this task. Through a comparative analysis of different NN models, we can provide guidance on selecting the most suitable model to enhance the effectiveness of NPF event classification.

Table 1

Measurement station and instrumentation supplying PNSD datasets to this study with location and type of environment.

City (country)	Station Name	Station type	Coordinates	Altitude
Budapest (Hungary)	BpART	Urban Background	47°28′30″N, 19°3′45″E	115m
Dresden (Germany)	Winckelmannstraβe	Urban Background	51°03′53″N, 13°44′29″E	120m
Leipzig (Germany)	TROPOS	Urban Background	51°21′9″N, 12°26′5″E	113m
Langen (Germany)	UBA	Urban Background	50°0′0″N, 8°23′24″E	130m
Dresden (Germany)	North	Traffic	51°05′13.7″N, 13°45′47″E	116m
Leipzig (Germany)	Mitte	Traffic	51°20′39″N, 12°22′38″E	111m
Leipzig (Germany)	Eisenbahnstrasse	Traffic	51°20′40.6″N, 12°25′20.6″E	120m
Ispra (Italy)	JRC	Regional Background	45°48′53″N, 8°38′9.9″ E	209m
Prague (Czech)	Suchdol	Suburban Background	50° 7′35″ N, 14° 23′5″ E	277m

Table 2
Instruments used to measure PNSD in the different stations. CPC, Condensation Particle Counter; DMPS, Differential Mobility Particle Sizer or Flow-switching Differential Mobility Particle Sizer; SMPS, Scanning Mobility Particle Sizer; TDMPS, Twin Differential Mobility Particle Sizer; TSMPS, Twin Scanning Mobility Particle Sizer; UCPC, Ultrafine Condensation Particle Counter.

Station Name	Availiable data	Data availability	Range (nm)
BUD_UB	DMPS + CPC TSI 3775	2013.11.13–2019.12.31	11–816
DRE_UB	TROPOS-SMPS uses a Vienna-type DMA 28 cm + CPC TSI 3772	2010.12.2–2019.12.31	10–800
LEI_UB	TROPOS-TDMPS uses a Vienna-type DMA 11 cm + UCPC TSI 3025	2009.1.1–2019.12.31	10–800
LAN_UB	SMPS TSI 3080 + TSI 3772, rebuild at TROPOS incl. software	2017.1.1–2019.12.31	10–544
DRE_TR	TROPOS-TSMPS uses a Vienna-type DMAs 11 cm and 28 cm + UCPC TSI 3025 and CPC TSI 3772	2017.1.1–2019.12.31	5–800
LEI_TR	TROPOS-TDMPS uses a Vienna-type DMA 11 cm + UCPC TSI 3025	2017.1.1–2019.12.31	10–800
LEI2_TR	TROPOS-TDMPS uses a Vienna-type DMA 11 cm + UCPC TSI 3025	2017.1.1–2019.12.31	10–800
ISP_RB	DMPS Vienna-type, home-made + CPCTSI 3010/3772	2017.1.1–2019.12.31	10–800
PRA_SUB	SMPS TSI 3034 rebuilt at TROPOS	2017.1.1–2019.12.31	11–478

2. Data and methods

2.1. Measurement sites, instrumentation and dataset

We examined an extensive dataset of PNSD over an extended period. This dataset contains nine monitoring sites, including four urban background sites (Budapest, BUD_UB, Dresden, DRE_UB, Leipzig, LEI_UB, and Langen, LAN_UB), three traffic sites (Dresden, DRE_TR, two sites in Leipzig, LEI_TR, LEI2_TR), one regional background site (Ispra, ISP_RB), and one suburban background site (Prague, PRA_SUB) as shown in Table 1.

To assemble the PNSD dataset, diverse instruments were employed, resulting in variations in the range of particle sizes that were measured as shown in Table 2. The instruments used were the Scanning Mobility Particle Sizer (SMPS), Differential Mobility Particle Sizer or Flow-switching Differential Mobility Particle Sizer (DMPS), Twin Scanning

Mobility Particle Sizer (TSMPS) or Twin Differential Mobility Particle Sizer (TDMPS). The Aerosol, Clouds and Trace Gases Research Infrastructure (ACTRIS) guidelines recommend a particle size measurement range of 10–800 nm (ACTRIS, 2021). However, for research purposes, especially in studying nucleation events, or due to equipment limitations, certain sites have measured PNSD in other sizes. At the BUD_UB site, the PNSD range of 10.8–816.2 nm considered in this study was extracted from the broader measured diameter interval, at the LAN_UB site, it is 10–543.7 nm, at the DRE_TR site, measurements start from 5.1 nm, and at the PRA_SUB site, the measurement range is 10.9–478.3 nm.

To ensure data quality, we conducted a number of data quality control procedures. We checked and corrected the time stamp of the data to ensure that all measurements were synchronized. We applied a data completeness filter to exclude data with poor availability. We also applied a quality filter to exclude data with unrealistic particle counts, such as those caused by instrument malfunction or ambient air contamination.

2.2. Classification of new particle formation events

Based on existing studies on NPF phenomenon (Baranizadeh et al., 2014; DAL MASO et al., 2005; Joutsensaari et al., 2018; Kulmala et al., 2012), the PNSD map in this study were classified into five different classes :

—Class E events (Class_E). A new mode appeared in the number spectrum distribution of the PNSD, and this new mode started to appear from the nuclear modal particle size range (3–25 nm) and showed an increasing trend.
—Class N events (Class_N) indicate the NPF, but no clear growth process can be observed. These events may also include days with weak growth.
—Nonevent days (Class_NE). Days with no NPF within the particle size range of the nucleation mode.
—Class unclear (Class_0). Some days do not meet the above classification criteria, and it is difficult to determine whether a NPF event has occurred since some but not all features for events can be seen.
—Bad Data (Class_BD). Days with missing or anomalous data due to instrument malfunction.

Fig. 1 portrays the diverse classes of NPF events. Class_E is regarded as clear event class due to the evident visibility of all stages in the process of NPF. In contrast, Class_N comprises days where evidence of NPF is observable, but the growth of particles is not clearly evident. For instance, NPF and their subsequent growth towards larger sizes may occur within a short time frame but then cease (e.g., due to sudden
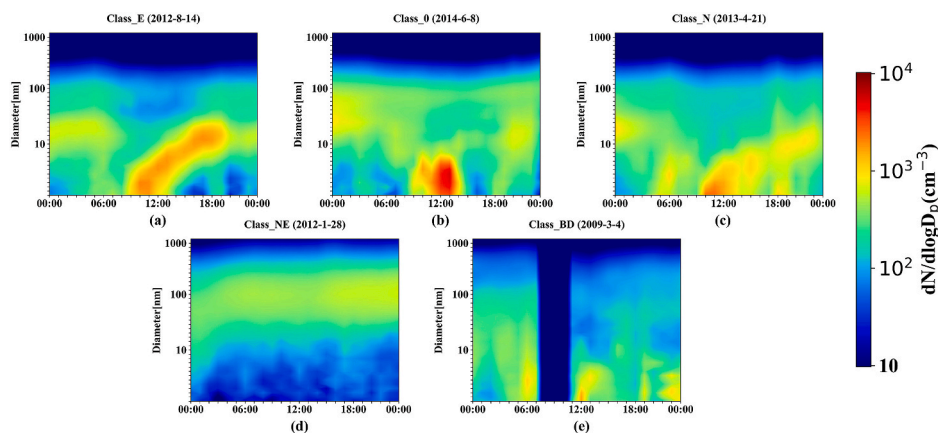
Fig. 1. Examples of different NPF event types (x-axis is time, y-axis is particle size, different colors indicate the number concentration of particles). (a) Class_E. (b) Class_0. (c) Class_N. (d) Class_NE. (e) Class_BD.

Table 3
Results of NPF dataset based on manual categorization and division of days to training (using the 80% dataset) and testing (using the remaining 20%).

Event class	Total days	Percentage of days (%)	Training 80%	Testing 20%
Class_E	842	25	674	168
Class_N	537	16	430	107
Class_NE	1031	31	825	206
Class_0	536	16	429	107
Class_BD	422	12	338	84
Total	3368	100	2696	672

meteorological changes or rainfall). Additionally, this category includes days when new particles do not grow to the Aitken mode size range (25–100nm).

In order to address the deficiencies and constraints posed by limited data samples, and consequently enhance the model's versatility across diverse scenarios, a pivotal strategy was adopted: the amalgamation and consolidation of data obtained from the three distinct sites (BUD_UB, DRE_UB, LEI_UB). By undertaking this amalgamation process, the model gains an enhanced ability to apprehend both shared attributes and distinctive aspects among the various sites, thus enabling it to adeptly navigate the intricacies of change and unpredictability inherent in real-world dynamics. The dataset was manually categorized by three experts using the aforementioned classification criteria. In cases where there was disagreement among the three experts, a fourth expert was consulted for classification. If the classification result matched that of one of the previous experts, that result was chosen. If the result did not match any of the previous three experts' results, it was categorized as Class_0. Across all monitoring sites, NPF event days represented 8.6% (BUD_UB), 4.1% (DRE_UB), 7.2% (LEI_UB), 0.9% (LAN_UB), 4.1% (DRE_TR), 5.3% (LEI_TR), 5.1% (LEI2_TR), 2.6% (ISP_RB) and 4.3%(PRA_SUB) of the total monitoring duration at their respective locations. Throughout the study, a subset of 3368 images with high confidence were chosen from the comprehensive dataset for research purposes. To better capture the image features of event days, we applied a twofold data augmentation to the event day data, employing techniques such as translation, scaling, and cropping. Among these, 80% of the images were dedicated to model training, while the remaining 20% were allocated for model testing (Table 3). Apart from the data from the three sites used for model training, the data from the remaining sites was specifically utilized to assess the model's generalization capabilities.

2.3. ConvNeXt model

The ConvNeXt model borrows features from the Swin Transformer architecture and summarizes the improvements to the convolutional neural network (CNN) (here the authors choose ResNet-50) into five parts, namely Macro Design, ResNeXt-ify, Inverted Bottleneck, Large Kernel Sizes, and Micro Design, using all existing structures and methods

(Liu et al., 2022). The model receives a PNSD image as input data and extracts its RGB values. In implementing the network structure, we used a pre-trained model and options (Epochs: 10; Batch Size: 8; Learning Rate: 0.0001; Weight Decay: 0.0009; Optimization Functions: AdamW). Its specific network structure is shown in Fig. 2.

Derived from the standard ResNet-50 and inspired by the Swin Transformer implementation, the network architecture has undergone modernization through five distinct enhancements.

Macro Design: The number of convolutional stages stacked in ResNet is modified to 3:3:9:3 (i.e., 1:1:3:1). At the same time, they borrowed the downsampling strategy of Swin Transformer and replaced the previous Resnet-style stem cell downsampling strategy with a convolutional layer of size 4x4 and step size 4.

ResNeXt-ify: The method borrowed from ResNeXt (S.N. Xie et al., 2017) introduces deep convolution (a type of grouped convolution) and increases the number of channels of the convolution kernel to the same number of channels as Swin Transformer.

Inverted Bottleneck: as shown in Fig. 3, the bottleneck structure in ResNext is thick at both ends and thin in the middle (i.e., the number of middle channels is small while the number of upper and lower channels is large), while the MLP module in the Transformer block and the Inverted bottleneck module in MobileNetV2 (Sandler et al., 2018) are similar in that they are both thin at both ends and thick in the middle, so the latter structure is also used in the proposed method.

Large Kernel Sizes: The convolutional kernel size of the network is enlarged to 7X7. Also, similar to the Transformer where the multi-headed self-attentive mechanism is placed before the MLP module, the authors reduce the overall computational effort by moving the deep convolutional operations up in the network.

Micro Design: The activation function and the normalization layer in the original network are removed, and only one activation function between two 1x1 convolutional layers is retained. The original RELU activation function and the original BatchNorm (BN) are replaced by GELU and Layer Normalization (LN) respectively.

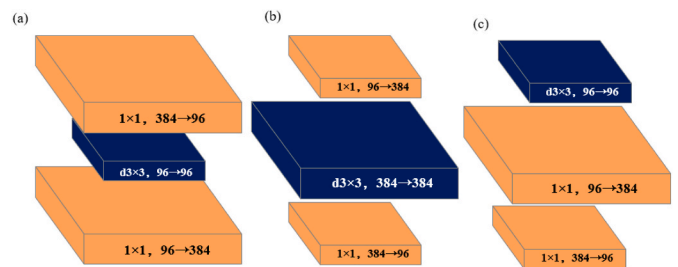In this study, we used the cross-validation (CV) method that used

Fig. 3. Reverse bottleneck structure schematic. (a) is a ResNeXt block; in (b), an inverted bottleneck block is created, and in (c), the position of the spatial depthwise conv layer is moved up.
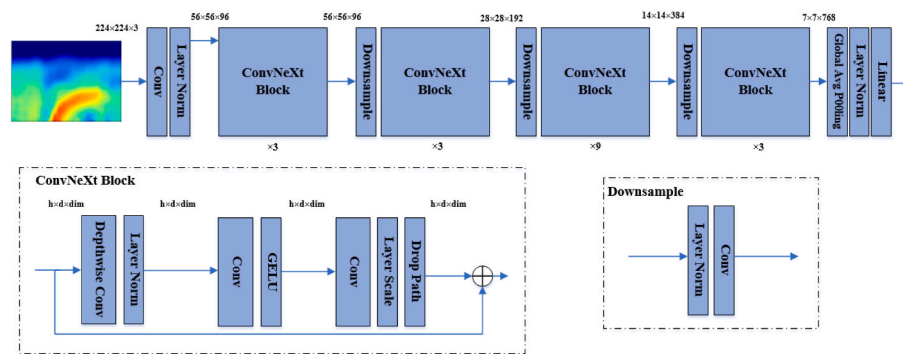

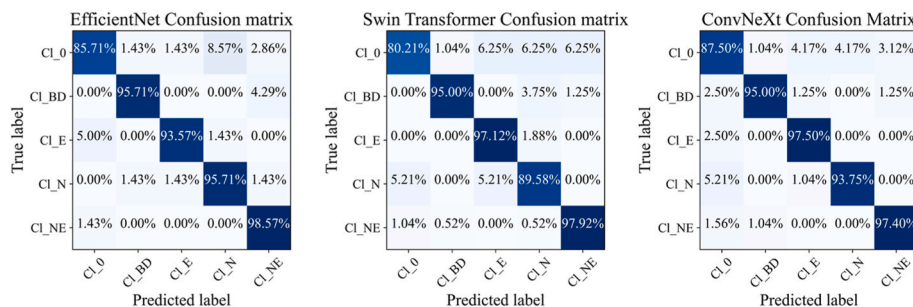**Fig. 2.** ConvNeXt-T model structure.

Fig. 4. Confusion matrix results for a single run on the test set.

80% of the monitoring data as the training data, and the 10-fold CV method to estimate the accuracy of the model. Furthermore, we conducted a comparative analysis involving two other deep learning models that have demonstrated exceptional performance on the ImageNet dataset in recent years: Swin Transformer and EfficientNet (details provided in the Supporting Material). Simultaneously, we applied transfer learning techniques (Shin et al., 2016; Tan et al., 2018; Yosinski et al., 2014) to fine-tune the initial three NNs, enhancing their capability to classify NPF events.

2.4. Statistical analysis

Data processing and statistical analyses were performed using Pycharm software (professional version 2022.2.2) and Python (v3.8.15). The model construction was carried out using the PyTorch framework (v2.0, cuda 11.8). Various libraries were employed in the data processing phase, including PIL (v8.4.0), pandas (v1.2.3), openCV (v4.8.1), and matplotlib (v3.5.3).

3. Results and discussion

3.1. Neural network classification

In this study, a single run of the three models on the test set was performed using the confusion matrix (Fig. 4), a widely used tool when evaluating specific computer vision models (Li and Deng, 2019; Nawwar et al., 2021). The highest event-day recognition accuracy for the three models was achieved by the ConvNeXt model (97.5%), followed by the Swin Transformer (97.12%) and the EfficientNet (93.57%). This is due to ConvNeXt's greater ability to capture complex features in the dataset as it has more parameters and inherits the benefits of traditional CNN, including built-in features such as bias, sliding window and translation invariance (Mauricio et al., 2023). At the same time, due to the depth-wise convolution used in the ConvNeXt network being performed independently on each channel, the network operates without involving channel-wise mixing operations. This helps preserve the spatial information of the input feature map, enabling the model to better capture local patterns in images. The Inverted Bottleneck structure contributes to preserving high-level representations of features, resulting in less information loss after passing through the activation function. Liu et al. (2023) used the ConvNeXt network to classify Chest X-ray (CXR) images, which adjusted the network structure and loss function, and found that the improved ConvNeXt network had better performance compared to other classical CNN networks.

The ConvNeXt model architecture, in terms of design philosophy, originates from ResNet and progressively integrates design concepts from recent ViT architectures, creating a novel pure convolutional network structure. The model comprehensively improves upon ResNet at both macro and micro levels and has been extensively experimentally validated for its superior performance. With the same FLOPS (Floating Point Operations Per Second), ConvNeXt has faster inference speed and higher classification accuracy than Swin Transformer.

Table 4
Performance of the three models on the test set (Image size is 224×224).

NPF type	ConvNeXt	Swin Transformer	EfficientNet
Class_E	**95.3**	94.9	92.8
Class_N	88.5	82.1	86.6
Class_0	80.6	78.3	81.2
Class_NE	93.3	95.1	92.5
Class_BD	92.9	91.9	84.5
Total	**91**	89.9	88.5

In addition, the three models were executed 10 times on the test set and averaged the values (in order to evaluate the performance of the models in recognizing each category) (Table 4). Overall, the combined accuracy of the three models is 91% (ConvNeXt), 89.9% (Swin Transformer) and 88.5% (EfficientNet), representing a notable improvement over all previous studies related to deep learning in the recognition of NPF events (Joutsensaari et al., 2018; Su et al., 2022).

Specifically, these models showed the highest accuracy in categorizing Class_E and Class_NE, while the accuracy for Class_N and Class_0 was relatively low, and the accuracy rates for Class_BD was in the middle range. The high accuracy in Class_BD is mainly attributed to the distinctive features within the BD category, notably the prevalence of numerous missing data attributes. This distinction becomes particularly apparent when examining the granularity distribution graph (Fig. 1 e) when BD category becomes more distinguishable in comparison to the other classes, ultimately resulting in a higher accuracy rate. Low accuracy of Class_N and Class_0 may be due to their intricate images with complex texture, shape and spatial attributes. In addition, the similarity between certain classes also plays a role (Cimpoi et al., 2016). For example, the particle concentrations of Class_N and Class_0 remain low in the range above 700 nm. At the same time, in the smaller particle size range, there is a sudden influx of aerosol particles, which exhibit irregular shapes in the images (Fig. 1 b and c).

In order to accurately describe the differences between classes, it has been proposed to designate clear event days and weak event days as quantizable and non-quantizable days (Baranizadeh et al., 2014), to make the classification results of human and deep learning models more consistent. Therefore, the results of this study showed that the recognition accuracies of ConvNeXt model on NPF event days and non-event days were 95.3% and 93.3%, respectively, while Swin Transformer and EfficientNet were 94.9%, 92.8% for event days and 95.1%, 92.5% for non-event days. This suggests that the ConvNeXt model's ability to accurately identify event days and non-event days approaches human classification performance. In addition, this again demonstrates the successful implementation of model migration learning.

3.2. Exploration of the ConvNeXt

To enhance the ConvNeXt model's precision in classifying NPF event days of Class_E, we conducted trials with various model scales on the dataset (change the number of channel per ConvNeXt Block and the

Table 5

ConvNeXt variants related information. C represents the number of input channels in the 4 stages and B represents the number of times the ConvNeXt Block was repeatedly stacked in each stage.

Variant type	C	B
ConvNeXt-T	(96, 192, 384, 768)	(3, 3, 9, 3)
ConvNeXt-S	(96, 192, 384, 768)	(3, 3, 27, 3)
ConvNeXt-B	(128, 256, 512, 1024)	(3, 3, 27, 3)
ConvNeXt-L	(192, 384, 768, 1536)	(3, 3, 27, 3)
ConvNeXt-XL	(256, 512, 1024, 2048)	(3, 3, 27, 3)

number of stacks (Liu et al., 2022), Specific information is shown in Table 5), subsequently undergoing training and testing, as outlined in Table 6. The experimental findings distinctly highlight that employing an expanded ConvNeXt model scale contributes to higher accuracy in classifying Class_E event days. The ConvNeXt-XL model achieves the best accuracy, achieving 97.8% accuracy on event days and 93.3% overall accuracy. Additionally, it is noteworthy that the model utilizing ImageNet 22k pre-training weights exhibits a marginally superior classification accuracy compared to its counterpart with ImageNet 1k pre-training weights (1k and 22k denote the number of classes in the ImageNet dataset).

By appropriately increasing the depth of the network, the ConvNeXt model can better capture abstract features and patterns in the image, thus improving performance on complex tasks (He et al., 2016; Szegedy et al., 2017; Tan and V. Le, 2020). In the intricate context of NPF events, employing a larger network proves effective in extracting finer-grained information from the data, thereby aiding the model in achieving more precise event recognition. Loading more intricate pre-training weights, such as those from ImageNet-22k, using the same model size, tends to

enhance event-day accuracy to some degree. A deeper network structure and a greater number of feature channels generally result in an expanded model parameter count, thereby enhancing the model's representational capacity (Khan et al., 2020). This augmentation facilitates the model in capturing more intricate and abstract features, empowering it to more effectively adapt to the intricacies of the training data. Compared to ConvNeXt-T, ConvNeXt-S/B/L/XL employs a deeper network structure and a higher number of feature channels, thus presenting superior performance in classification tasks.

From a data perspective, as observed in Fig. 5, it is evident that different categories share similar or identical features, making the features of images from distinct classes not entirely unique. Taking Class_BD as an example, its images encompass features present in Class_0. Additionally, there is positional occlusion among the features. Therefore, the model requires a greater number of parameters to discern these intricate scenarios.

3.3. Verification of generalizability

To assess the generalization performance of the ConvNeXt model, we conducted experiments utilizing ConvNeXt-XL at six sites: LAN_UB, DRE_TR, LEI_TR, LEI2_TR, ISP_RB, and PRA_SUB. The detailed results are presented in Table 7.

The event-day accuracies for each site are as follows: 75.0% (LAN_UB), 84.4% (DRE_TR), 86.2% (LEI_TR), 96.4% (LEI2_TR), 78.6% (ISP_RB), and 55.3% (PRA_SUB). These results underscore the exceptional generalization performance of our model in event-day recognition. It is noteworthy that a 10.2% difference exists between the results obtained from the LEI_TR and LEI2_TR sites. We attribute this discrepancy to disparities in external traffic and site surroundings, leading to
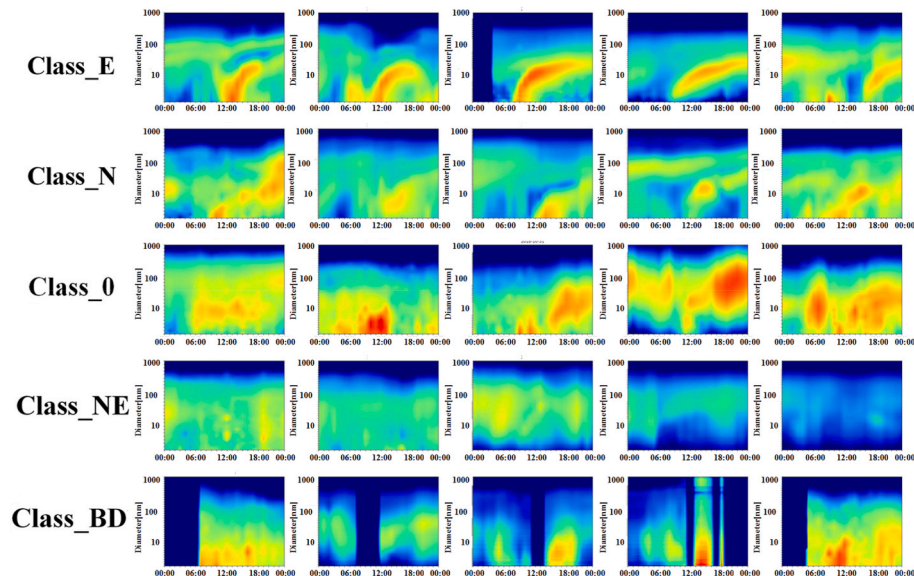
Table 6

Accuracy of the ConvNeXt model on the test set (Image size is 224 × 224); 1k and 22k denote the number of classes in the ImageNet dataset.

NPF type	ConvNeXt-T	ConvNeXt-S	ConvNeXt-B		ConvNeXt-L		ConvNeXt-XL
	1k	1k	1k	22k	1k	22k	22k
Class_E	95.3	95.9	96	96.3	96.7	97.2	**97.8**
Class_N	88.5	88.1	88	90.1	89.6	89.7	89.7
Class_0	80.6	82	84.4	82	83.4	85	83.2
Class_NE	93.3	94.2	94.4	95.1	95.6	89.9	91.1
Class_BD	92.9	92.7	91.7	93.9	95	96.4	96.9
Total	91	91.5	91.8	91.9	92.4	**93.5**	93.3

Fig. 5. Examples of data for each category in PNSD.

Table 7
Experimental results on the generalizability of the ConvNeXt-XL model.

Class label	LAN_UB	DRE_TR	LEI_TR	LEI2_TR	ISP_RB	PRA_SUB
Class_E	75	84.4	86.2	96.4	78.6	55.3
Class_N	46.2	44.8	31	40	54.5	37.9
Class_0	63.6	27.1	71.3	59.7	12.7	34.2
Class_NE	84.1	94.5	96.3	96.8	95.8	96.1
Class_BD	98.1	90	97.7	82.9	97.2	97.4
Total	76.1	59.2	81.1	68.5	48.8	59.2

distinctions in data features between the two sites. At the PRA_SUB site, the lower event day accuracy is attributed to the cleaner air in the site's vicinity, resulting in a substantial feature disparity between the site data and the model training data. The lower accuracy of model generalization for Class_0 vs. Class_N can be partially ascribed to variations in PNSD maps caused by differences in traffic, air quality, and geography between sites. Additionally, the model's need for more complex feature representations contributes to this discrepancy. The more complex features here are not limited to the "banana-like" nucleation process, but also include features such as the correlation of previous and later time events that the model can learn, as well as the overall pollution status of the station. Addressing these differences may necessitate a more in-depth analysis and refinement to enhance the model's generalization performance for these specific classes.

Due to their data-driven nature, the performance of deep learning models is highly reliant on the training data. The model's performance can vary across different datasets. When training the model using different datasets, it is essential to ensure the quality (i.e., the credibility of event-day classification results and the various forms of particle "nucleation-growth" on event days) and quantity of the data. Additionally, experimentation and adjustments may be necessary for hyperparameters like the learning rate.

4. Conclusions

This study designed a new deep learning method to automatically detect regional NPF events, which approaches the accuracy level of manual classification. The ConvNeXt model achieves 95.3% accuracy, followed by the swin Transformer and EfficientNet models with 94.9% and 92.8% accuracy, respectively. Furthermore, the ConvNeXt model performs best in downstream tasks (especially NPF event classification). The ConvNeXt-XL model achieved an even higher event-day accuracy of 97.8%. In the generalizability experiments, the event-day accuracy of the LEI2_TR site was particularly satisfactory, reaching 96.4%. The method exhibits robustness in accurately classifying PNSD obtained from various combinations of instruments and eliminates the need for cumbersome data processing. It largely avoids the subjectivity in the manual classification process and improves the credibility of the classification results. By utilizing a pre-trained image classification model, we can efficiently build an automated NPF event classification system through transfer learning, leveraging the powerful computational capabilities to manage the complexity and large-scale data in the field of atmospheric science.

CRediT authorship contribution statement

Xun Zhang: Conceptualization. **Lijie Wu:** Writing – original draft, Validation, Methodology, Conceptualization. **Xiansheng Liu:** Writing – original draft, Data curation. **Tao Wang:** Data curation. **Marta Monge:** Investigation. **Meritxell Garcia-Marlès:** Data curation. **Marjan Savadkoohi:** Data curation. **Imre Salma:** Data curation. **Susanne Bastian:** Data curation. **Maik Merkel:** Data curation. **Kay Weinhold:** Data curation. **Alfred Wiedensohler:** Data curation. **Holger Gerwig:** Data curation. **Jean Putaud:** Data curation. **Sebastiao Martins Dos Dantos:** Data curation. **Jakub Ondracek:** Data curation. **Nadezda**

Zikova: Data curation. **Andrea Minkos:** Data curation. **Marco Pandolfi:** Data curation. **Andrés Alastuey:** Data curation. **Xavier Querol:** Data curation.

Declaration of competing interest

The authors declare that they have no known competing financial interests or personal relationships that could have appeared to influence the work reported in this paper.

Data availability

Data will be made available on request.

Appendix A. Supplementary data

Supplementary data to this article can be found online at https://doi.org/10.1016/j.atmosenv.2024.120487.

References

ACTRIS, 2021. Preliminary ACTRIS Recommendation for Aerosol In-Situ Sampling, Measurements, and Analysis.

Almeida, J., Schobesberger, S., Kurten, A., Ortega, I.K., Kupiainen-Maatta, O., Praplan, A. P., Adamov, A., Amorim, A., Bianchi, F., Breitenlechner, M., David, A., Dommen, J., Donahue, N.M., Downard, A., Dunne, E., Duplissy, J., Ehrhart, S., Flagan, R.C., Franchin, A., Guida, R., Hakala, J., Hansel, A., Heinritzi, M., Henschel, H., Jokinen, T., Junninen, H., Kajos, M., Kangasluoma, J., Keskinen, H., Kupc, A., Kurten, T., Kvashin, A.N., Laaksonen, A., Lehtipalo, K., Leiminger, M., Leppa, J., Loukonen, V., Makhmutov, V., Mathot, S., McGrath, M.J., Nieminen, T., Olenius, T., Onnela, A., Petaja, T., Riccobono, F., Riipinen, I., Rissanen, M., Rondo, L., Ruuskanen, T., Santos, F.D., Sarnela, N., Schallhart, S., Schnitzhofer, R., Seinfeld, J. H., Simon, M., Sipila, M., Stozhkov, Y., Stratmann, F., Tome, A., Trostl, J., Tsagkogeorgas, G., Vaattovaara, P., Viisanen, Y., Virtanen, A., Vrtala, A., Wagner, P. E., Weingartner, E., Wex, H., Williamson, C., Wimmer, D., Ye, P.L., Yli-Juuti, T., Carslaw, K.S., Kulmala, M., Curtius, J., Baltensperger, U., Worsnop, D.R., Vehkamaki, H., Kirkby, J., 2013. Molecular understanding of sulphuric acid-amine particle nucleation in the atmosphere. Nature 502, 359.

Alonso-Blanco, E., Gómez-Moreno, F.J., Artíñano, B., Iglesias-Samitier, S., Juncal-Bello, V., Piñeiro-Iglesias, M., López-Mahía, P., Pérez, N., Brines, M., Alastuey, A., 2018. Temporal and spatial variability of atmospheric particle number size distributions across Spain. Atmos. Environ. 190, 146–160, 1994.

Baranizadeh, E., Arola, A., Hamed, A., Nieminen, T., Mikkonen, S., Virtanen, A., Kulmala, M., Lehtinen, K., Laaksonen, A., 2014. The effect of cloudiness on new-particle formation: investigation of radiation levels. Boreal Environ. Res. 19, 343–354.

Beck, L.J., Sarnela, N., Junninen, H., Hoppe, C.J.M., Garmash, O., Bianchi, F., Riva, M., Rose, C., Peräkylä, O., Wimmer, D., Kausiala, O., Jokinen, T., Ahonen, L., Mikkilä, J., Hakala, J., He, X.C., Kontkanen, J., Wolf, K.K.E., Cappelletti, D., Mazzola, M., Traversi, R., Petroselli, C., Viola, A.P., Vitale, V., Lange, R., Massling, A., Nøjgaard, J. K., Krejci, R., Karlsson, L., Zieger, P., Jang, S., Lee, K., Vakkari, V., Lampilahti, J., Thakur, R.C., Leino, K., Kangasluoma, J., Duplissy, E.M., Siivola, E., Marbouti, M., Tham, Y.J., Saiz Lopez, A., Petäjä, T., Ehn, M., Worsnop, D.R., Skov, H., Kulmala, M., Kerminen, V.M., Sipilä, M., 2021. Differing mechanisms of new particle formation at two arctic sites. Geophys. Res. Lett. 48.

Cai, R.L., Jiang, J.K., 2017. A new balance formula to estimate new particle formation rate: reevaluating the effect of coagulation scavenging. Atmos. Chem. Phys. 17, 12659–12675.

Carnerero, C., Rivas, I., Reche, C., Pérez, N., Alastuey, A., Querol, X., 2021. Trends in primary and secondary particle number concentrations in urban and regional environments in NE Spain. Atmos. Environ. 244, 117982, 1994.

Chu, B., Kerminen, V., Bianchi, F., Yan, C., Petäjä, T., Kulmala, M., 2019. Atmospheric new particle formation in China. Atmos. Chem. Phys. 19, 115–138.

Cimpoi, M., Maji, S., Kokkinos, I., Vedaldi, A., 2016. Deep filter banks for texture recognition, description, and segmentation. Int. J. Comput. Vis. 118, 65–94.

Dada, L., Chellapermal, R., Buenrostro Mazon, S., Paasonen, P., Lampilahti, J., Manninen, H.E., Junninen, H., Petäjä, T., Kerminen, V., Kulmala, M., 2018. Refined classification and characterization of atmospheric new-particle formation events using air ions. Atmos. Chem. Phys. 18, 17883–17893.

Dal Maso, M., Kulmala, M., Riipinen, I., Wagner, R., Hussein, T., Aalto, P.P., Lehtinen, K. E.J., 2005. Formation and growth of fresh atmospheric aerosols : eight years of aerosol size distribution data from SMEAR II, Hyytiälä, Finland. Boreal Environ. Res. 10, 323–336.

Deng, J., Dong, W., Socher, R., Li, L.J., Li, K., Li, F.F., Ieee, 2009. ImageNet: a large-scale hierarchical image database. CVPR: 2009 IEEE CONFERENCE on COMPUTER VISION and PATTERN RECOGNITION, VOLS 1-4, IEEE-Computer-Society Conference on Computer Vision and Pattern Recognition Workshops, pp. 248–255.

Du, W., Dada, L., Zhao, J., Chen, X.S., Daellenbach, K.R., Xie, C.H., Wang, W.G., He, Y., Cai, J., Yao, L., Zhang, Y.J., Wang, Q.Q., Xu, W.Q., Wang, Y.Y., Tang, G.Q., Cheng, X. L., Kokkonen, T.V., Zhou, W., Yan, C., Chu, B.W., Zha, Q.Z., Hakala, S., Kurppa, M., Jarvi, L., Liu, Y.C., Li, Z.Q., Ge, M.F., Fu, P.Q., Nie, W., Bianchi, F., Petaja, T., Paasonen, P., Wang, Z.F., Worsnop, D.R., Kerminen, V.M., Kulmala, M., Sun, Y.L., 2021. A 3D study on the amplification of regional haze and particle growth by local emissions. NPJ Clim Atmos Sci 4.

Ehn, M., Thornton, J.A., Kleist, E., Sipila, M., Junninen, H., Pullinen, I., Springer, M., Rubach, F., Tillmann, R., Lee, B., Lopez-Hilfiker, F., Andres, S., Acir, I.H., Rissanen, M., Jokinen, T., Schobesberger, S., Kangasluoma, J., Kontkanen, J., Nieminen, T., Kurten, T., Nielsen, L.B., Jorgensen, S., Kjaergaard, H.G., Canagaratna, M., Dal Maso, M., Berndt, T., Petaja, T., Wahner, A., Kerminen, V.M., Kulmala, M., Worsnop, D.R., Wildt, J., Mentel, T.F., 2014. A large source of low-volatility secondary organic aerosol. Nature 506, 476.

Hamed, A., Joutsensaari, J., Mikkonen, S., Sogacheva, L., Dal Maso, M., Kulmala, M., Cavalli, F., Fuzzi, S., Facchini, M.C., Decesari, S., Mircea, M., Lehtinen, K., Laaksonen, A., 2007. Nucleation and growth of new particles in Po Valley, Italy. Atmos. Chem. Phys. 7, 355–376.

He, K.M., Zhang, X.Y., Ren, S.Q., Sun, J., 2016. Identity mappings in deep residual networks. In: Leibe, B., Matas, J., Sebe, N., Welling, M. (Eds.), COMPUTER VISION - ECCV 2016, PT IV, 14th European Conference on Computer Vision. ECCV), pp. 630–645.

Hopke, P.K., Feng, Y.C., Dai, Q.L., 2022. Source apportionment of particle number concentrations: a global review. Sci. Total Environ. 819.

Joutsensaari, J., Ozon, M., Nieminen, T., Mikkonen, S., Lähivaara, T., Decesari, S., Facchini, M.C., Laaksonen, A., Lehtinen, K.E.J., 2018. Identification of new particle formation events with deep learning. Atmos. Chem. Phys. 18, 9597–9615.

Kecorius, S., Zhang, S., Wang, Z., Groess, J., Ma, N., Wu, Z., Ran, L., Hu, M., Wang, P., Ulevicius, V., Wiedensohler, A., 2015. Nocturnal aerosol particle formation in the north China plain. Lith. J. Phys. 55, 44–53.

Khan, A., Sohail, A., Zahoora, U., Qureshi, A.S., 2020. A survey of the recent architectures of deep convolutional neural networks. Artif. Intell. Rev. 53, 5455–5516.

Kulmala, M., 2003. How particles nucleate and grow. Science 302, 1000–1001.

Kulmala, M., Kontkanen, J., Junninen, H., Lehtipalo, K., Manninen, H.E., Nieminen, T., Petaja, T., Sipila, M., Schobesberger, S., Rantala, P., Franchin, A., Jokinen, T., Jarvinen, E., Aijala, M., Kangasluoma, J., Hakala, J., Aalto, P.P., Paasonen, P., Mikkila, J., Vanhanen, J., Aalto, J., Hakola, H., Makkonen, U., Ruuskanen, T., Mauldin, R.L., Duplissy, J., Vehkamaki, H., Back, J., Kortelainen, A., Riipinen, I., Kurten, T., Johnston, M.V., Smith, J.N., Ehn, M., Mentel, T.F., Lehtinen, K., Laaksonen, A., Kerminen, V.M., Worsnop, D.R., 2013. Direct observations of atmospheric aerosol nucleation. Science 339, 943–946.

Kulmala, M., Lehtinen, K., Laaksonen, A., 2006. Cluster activation theory as an explanation of the linear dependence between formation rate of 3nm particles and sulphuric acid concentration. Atmos. Chem. Phys. 6, 787–793.

Kulmala, M., Petaja, T., Nieminen, T., Sipila, M., Manninen, H.E., Lehtipalo, K., Dal Maso, M., Aalto, P.P., Junninen, H., Paasonen, P., Riipinen, I., Lehtinen, K., Laaksonen, A., Kerminen, V.M., 2012. Measurement of the nucleation of atmospheric aerosol particles. Nat. Protoc. 7, 1651–1667.

Kulmala, M., Pirjola, U., Makela, J.M., 2000. Stable sulphate clusters as a source of new atmospheric particles. Nature 404, 66–69.

Lehtipalo, K., Yan, C., Dada, L., Bianchi, F., Xiao, M., Wagner, R., Stolzenburg, D., Ahonen, L.R., Amorim, A., Baccarini, A., Bauer, P.S., Baumgartner, B., Bergen, A., Bernhammer, A.K., Breitenlechner, M., Brilke, S., Buchholz, A., Mazon, S.B., Chen, D.X., Chen, X.M., Dias, A., Dommen, J., Draper, D.C., Duplissy, J., Ehn, M., Finkenzeller, H., Fischer, L., Frege, C., Fuchs, C., Garmash, O., Gordon, H., Hakala, J., He, X.C., Heikkinen, L., Heinritzi, M., Helm, J.C., Hofbauer, V., Hoyle, C. R., Jokinen, T., Kangasluoma, J., Kerminen, V.M., Kim, C., Kirkby, J., Kontkanen, J., Kurten, A., Lawler, M.J., Mai, H.J., Mathot, S., Mauldin, R.L., Molteni, U., Nichman, L., Nie, W., Nieminen, T., Ojdanic, A., Onnela, A., Passananti, M., Petaja, T., Piel, F., Pospisilova, V., Quelever, L., Rissanen, M.P., Rose, C., Sarnela, N., Schallhart, S., Schuchmann, S., Sengupta, K., Simon, M., Sipila, M., Tauber, C., Tome, A., Trostl, J., Vaisanen, O., Vogel, A.L., Volkamer, R., Wagner, A.C., Wang, M. Y., Weitz, L., Wimmer, D., Ye, P.L., Ylisirnio, A., Zha, Q.Z., Carslaw, K.S., Curtius, J.,

Donahue, N.M., Flagan, R.C., Hansel, A., Riipinen, I., Virtanen, A., Winkler, P.M., Baltensperger, U., Kulmala, M., Worsnop, D.R., 2018. Multicomponent new particle formation from sulfuric acid, ammonia, and biogenic vapors. Sci. Adv. 4.

Lelieveld, J., Klingmüller, K., Pozzer, A., Pöschl, U., Fnais, M., Daiber, A., Münzel, T., 2019. Cardiovascular disease burden from ambient air pollution in Europe reassessed using novel hazard ratio functions. Eur. Heart J. 40, 1590–1596.

Li, S., Deng, W.H., 2019. Blended emotion in-the-Wild: multi-label facial expression recognition using crowdsourced annotations and deep locality feature learning. Int. J. Comput. Vis. 127, 884–906.

Lihavainen, H., Kerminen, V.M., Komppula, M., Hatakka, J., Aaltonen, V., Kulmala, M., Viisanen, Y., 2003. Production of "potential" cloud condensation nuclei associated with atmospheric new-particle formation in northern Finland. J. Geophys. Res. Atmos. 108 n/a-n/a.

Liu, F.X., Zang, C., Shi, J.Q., He, W.Y., Li, L., Liang, Y.P., 2023. An improved COVID-19 lung X-ray image classification algorithm based on ConvNeXt network. Int. J. Image Graph.

Liu, Z., Lin, Y.T., Cao, Y., Hu, H., Wei, Y.X., Zhang, Z., Lin, S., Guo, B.N., Ieee, 2021. Swin transformer: hierarchical vision transformer using shifted windows. In: 2021 IEEE/ CVF INTERNATIONAL CONFERENCE on COMPUTER VISION (ICCV 2021), 18th IEEE/CVF International Conference on Computer Vision (ICCV), pp. 9992–10002.

Liu, Z., Mao, H.Z., Wu, C.Y., Feichtenhofer, C., Darrell, T., Xie, S.N., Ieee, C.S., 2022. A ConvNet for the 2020s. 2022 IEEE/CVF CONFERENCE on COMPUTER VISION and PATTERN RECOGNITION (CVPR), IEEE/CVF Conference on Computer Vision and Pattern Recognition (CVPR), pp. 11966–11976.

Luo, H., Guan, Q., Lin, J., Wang, Q., Yang, L., Tan, Z., Wang, N., 2020. Air pollution characteristics and human health risks in key cities of northwest China. J. Environ. Manag. 269, 110791.

Mauricio, J., Domingues, I., Bernardino, J., 2023. Comparing vision transformers and convolutional neural networks for image classification: a literature review. Appl. Sci. 13.

Napari, I., Kulmala, M., Vehkamaki, H., 2002. Ternary nucleation of inorganic acids, ammonia, and water. J. Chem. Phys. 117, 8418–8425.

Nawwar, N.M., Kasban, H., Salama, M., 2021. Improvement of confusion matrix for hand vein recognition based on deep- learning multi-classifier decisions. Arab J Nucl Sci Appl 54, 135–148.

Park, J.U., Kim, H.J., Choi, J., Park, J.S., Heo, J., Kim, S.W., 2021. Observation of aerosol size distribution and new particle formation under different air masses arriving at the northwesternmost South Korean island in the Yellow Sea. Atmos. Res. 255.

Pierce, J.R., Westervelt, D.M., Atwood, S.A., Barnes, E.A., Leaitch, W.R., 2014. New-particle formation, growth and climate-relevant particle production in Egbert, Canada: analysis from 1 year of size-distribution observations. Atmos. Chem. Phys. 14, 8647–8663.

Rivas, I., Beddows, D., Amato, F., Green, D.C., Jarvi, L., Hueglin, C., Reche, C., Timonen, H., Fuller, G.W., Niemi, J.V., Perez, N., Aurela, M., Hopke, P.K., Alastuey, A., Kulmala, M., Harrison, R.M., Querol, X., Kelly, F.J., 2020. Source apportionment of particle number size distribution in urban background and traffic stations in four European cities. Environ. Int. 135.

Rosenfeld, D., Lohmann, U., Raga, G.B., O'Dowd, C.D., Kulmala, M., Fuzzi, S., Reissell, A., Andreae, M.O., 2008. Flood or drought: how do aerosols affect precipitation? Science 321, 1309–1313.

Salimi, F., Ristovski, Z., Mazaheri, M., Laiman, R., Crilley, L.R., He, C., Clifford, S., Morawska, L., 2014. Assessment and application of clustering techniques to atmospheric particle number size distribution for the purpose of source apportionment. Atmos. Chem. Phys. 14, 11883–11892.

Salma, I., Thén, W., Aalto, P., Kerminen, V.-M., Kern, A., Barcza, Z., Petäjä, T., Kulmala, M., 2021. Influence of vegetation on occurrence and time distributions of regional new aerosol particle formation and growth. Atmos. Chem. Phys. 21, 2861–2880.

Sandler, M., Howard, A., Zhu, M.L., Zhmoginov, A., Chen, L.C., Ieee, 2018. MobileNetV2: inverted residuals and linear bottlenecks. In: 2018 IEEE/CVF CONFERENCE on COMPUTER VISION and PATTERN RECOGNITION (CVPR), 31st IEEE/CVF Conference on Computer Vision and Pattern Recognition (CVPR), pp. 4510–4520.

Shin, H.C., Roth, H.R., Gao, M.C., Lu, L., Xu, Z.Y., Nogues, I., Yao, J.H., Mollura, D., Summers, R.M., 2016. Deep convolutional neural networks for computer-aided detection: CNN architectures, dataset characteristics and transfer learning. IEEE Trans. Med. Imag. 35, 1285–1298.

Su, P., Joutsensaari, J., Dada, L., Zaidan, M.A., Nieminen, T., Li, X., Wu, Y., Decesari, S., Tarkoma, S., Petäjä, T., Kulmala, M., Pellikka, P., 2022. New particle formation event detection with Mask R-CNN. Atmos. Chem. Phys. 22, 1293–1309.

Szegedy, C., Ioffe, S., Vanhoucke, V., Alemi, A.A., Aaai, 2017. Inception-v4, inception-ResNet and the impact of residual connections on learning. In: THIRTY-FIRST AAAI CONFERENCE on ARTIFICIAL INTELLIGENCE, 31st AAAI Conference on Artificial Intelligence, pp. 4278–4284.

Tan, C., Sun, F., Kong, T., Zhang, W., Yang, C., Liu, C., 2018. A Survey on Deep Transfer Learning. Arxiv.

Tan, M., Le, Q.V., 2020. EfficientNet: Rethinking Model Scaling for Convolutional Neural Networks. Arxiv.

Trechera, P., Garcia-Marlès, M., Liu, X., Reche, C., Pérez, N., Savadkoohi, M., Beddows, D., Salma, I., Vörösmarty, M., Casans, A., 2023. Phenomenology of ultrafine particle concentrations and size distribution across urban Europe. Environ. Int. 172, 107744.

Vana, M., Ehn, M., Petäjä, T., Vuollekoski, H., Aalto, P., de Leeuw, G., Ceburnis, D., O'Dowd, C.D., Kulmala, M., 2008. Characteristic features of air ions at Mace Head on the west coast of Ireland. Atmos. Res. 90, 278–286.

Vörösmarty, M., Hopke, P.K., Salma, I.. Attribution of aerosol particle number size distributions to major sources using a 11-year-long urban dataset, EGUsphere [preprint]. https://doi.org/10.5194/egusphere-2024-316.

Wang, Y.H., Liu, Z.R., Zhang, J.K., Hu, B., Ji, D.S., Yu, Y.C., Wang, Y.S., 2015. Aerosol physicochemical properties and implications for visibility during an intense haze episode during winter in Beijing. Atmos. Chem. Phys. 15, 3205–3215.

WHO, 2021. WHO Global Air Quality Guidelines: Particulate Matter (PM2.5 and PM10), Ozone, Nitrogen Dioxide, Sulfur Dioxide and Carbon Monoxide. World Health Organization. https://apps.who.int/iris/handle/10665/345329. CC BY-NC-SA 3.0 IGO.

Xie, H.B., Elm, J., Halonen, R., Myllys, N., Kurten, T., Kulmala, M., Vehkamaki, H., 2017. Atmospheric fate of monoethanolamine: enhancing new particle formation of sulfuric acid as an important removal process. Environ. Sci. Technol. 51, 8422–8431.

Xie, S.N., Girshick, R., Dollar, P., Tu, Z.W., He, K.M., Ieee, 2017. Aggregated residual transformations for deep neural networks. 30TH IEEE CONFERENCE on COMPUTER VISION and PATTERN RECOGNITION (CVPR 2017), 30th IEEE/CVF Conference on Computer Vision and Pattern Recognition (CVPR), pp. 5987–5995.

Yosinski, J., Clune, J., Bengio, Y., Lipson, H., 2014. How transferable are features in deep neural networks. In: Ghahramani, Z., Welling, M., Cortes, C., Lawrence, N.D., Weinberger, K.Q. (Eds.), ADVANCES IN NEURAL INFORMATION PROCESSING SYSTEMS 27 (NIPS 2014), 28th Conference on Neural Information Processing Systems. NIPS).

Yue, D.L., Hu, M., Zhang, R.Y., Wang, Z.B., Zheng, J., Wu, Z.J., Wiedensohler, A., He, L. Y., Huang, X.F., Zhu, T., 2010. The roles of sulfuric acid in new particle formation and growth in the mega-city of Beijing. Atmos. Chem. Phys. 10, 4953–4960.

Zaidan, M.A., Haapasilta, V., Relan, R., Junninen, H., Aalto, P.P., Kulmala, M., Laurson, L., Foster, A.S., 2018. Predicting atmospheric particle formation days by Bayesian classification of the time series features. Tellus Ser. B Chem. Phys. Meteorol. 70.

Zhang, Q., Zheng, Y.X., Tong, D., Shao, M., Wang, S.X., Zhang, Y.H., Xu, X.D., Wang, J. N., He, H., Liu, W.Q., Ding, Y.H., Lei, Y., Li, J.H., Wang, Z.F., Zhang, X.Y., Wang, Y. S., Cheng, J., Liu, Y., Shi, Q.R., Yan, L., Geng, G.N., Hong, C.P., Li, M., Liu, F., Zheng, B., Cao, J.J., Ding, A.J., Gao, J., Fu, Q.Y., Huo, J.T., Liu, B.X., Liu, Z.R., Yang, F.M., He, K.B., Hao, J.M., 2019. Drivers of improved PM2.5 air quality in China from 2013 to 2017. Proc. Natl. Acad. Sci. U. S. A. 116, 24463–24469.

Zhang, R.Y., 2010. Getting to the critical nucleus of aerosol formation. Science 328, 1366–1367.

Zhang, R.Y., Khalizov, A., Wang, L., Hu, M., Xu, W., 2012. Nucleation and growth of nanoparticles in the atmosphere. Chem. Rev. 112, 1957–2011.

Zhang, R.Y., Suh, I., Zhao, J., Zhang, D., Fortner, E.C., Tie, X.X., Molina, L.T., Molina, M. J., 2004. Atmospheric new particle formation enhanced by organic acids. Science 304, 1487–1490.

Zhong, J.T., Zhang, X.Y., Wang, Y.Q., Sun, J.Y., Zhang, Y.M., Wang, J.Z., Tan, K.Y., Shen, X.J., Che, H.C., Zhang, L., Zhang, Z.X., Qi, X.F., Zhao, H.R., Ren, S.X., Li, Y., 2017. Relative contributions of boundary-layer meteorological factors to the explosive growth of PM2.5 during the red-alert heavy pollution episodes in Beijing in december 2016. J Meteorol Res 31, 809–819.